A robust super-resolution method with improved high-frequency components estimation and aliasing correction capabilities ☆

Baraka Maiseli[a,b,*], Chuan Wu[c], Jiangyuan Mei[a], Qiang Liu[a], Huijun Gao[a]

[a]*Research Institute of Intelligent Control and Systems, Harbin Institute of Technology, Harbin 150001, PR China*
[b]*University of Dar es Salaam, College of Information & Communication Technology, Department of Electronics & Telecommunication Engineering, P.O. Box 35194, Dar es Salaam, Tanzania*
[c]*Key Laboratory of Airborne Optical Imaging and Measurement, Image Processing Laboratory, Changchun Institute of Optics, Fine Mechanics and Physics, Chinese Academy of Sciences, Changchun 130033, PR China*

Abstract

In this paper, we have proposed a robust super-resolution high-frequency component estimation (RS-HFCE) method, which can efficiently estimate lost high-frequency components and correct aliasing effects of low-frequency components of an image. The fundamental principle of operation of the proposed method is based on the idea that, when a baseband band-limited image signal of known bandwidth in a high-resolution lattice is iteratively low-pass filtered in the frequency domain, the unknown values in the lattice can be interpolated, thus correcting the aliasing for the low-frequency components. If this process is done along with adjusting the amplitudes of the known pixel values, some high-frequency components of an image are automatically extrapolated. In order to provide simultaneous edge preservation and noise removal capabilities of the super-resolved images, an improved version of an adaptive Perona–Malik (PM) model is incorporated into the process. One of the characteristics of the proposed method is its high level of tolerance capabilities to reconstruction errors and noise caused by an increase in the reconstruction scaling factors. High quality images of higher resolution are still appreciably reconstructed when greater magnification factors are used. From a couple of experiments on real images, and using both subjective and objective

image quality assessment measures, it is demonstrated that the proposed method outperforms most of other classical methods.

1. Introduction

1.1. A brief overview of the super-resolution technology

Super-resolution (SR), one of the most active and open-ended areas of research, can be defined as a digital image processing technology that can be used to reconstruct a High-Resolution (HR) image from at least one low-resolution (LR) image [1]. This branch of image processing closely relates to interpolation (see [2,3]) because it generally deals with enlargement and enhancement of low resolution and degraded images. There are a good number of applications of the SR technology. One of the typical applications of this technology can be observed in web browsers, where high resolution images and streaming videos are naturally required [4]. In the near future, we think the applications of the SR technology can be extended to the Engineering control feedback systems, so that the feedback information contains the super-resolved images rather than complicated networks (see [5–8]). Two main types of SR methods are known, namely classical multi-image SR, which involve reconstruction of a HR image from multiple LR images of the same scene but different sub-pixel alignment, and Example-Based SR, which deals with learning the correspondence between low and high resolution patches from a database [9]. Our paper implements a classical multi-image SR and, in the rest of the paper, SR refers to a classical multi-image super-resolution.

Generally, an SR problem can be broken down into two major parts: registration and reconstruction. Registration is the very early stage that involves acquisition of a sequence of images of the same scene, estimation of the relative motion parameters between each image and a reference image, and finally re-arrangement of the images into a sub-pixel grid using the calculated motion parameters. If an image to be registered is exactly the same in every aspect with the reference image, and all relative motion elements between this image and a reference image are zero, then registration is meaningless. However, with an assumption that there exist camera movements and time difference during image acquisition, the motion parameters are usually non-zero entities, thereby making registration necessary. Registration is a critical stage to the overall success of reconstruction of a HR scene [10]. The reconstruction process follows just after the registration process. Here, the information available on a sub-pixel grid is directly projected on a high resolution grid. Additional processes which are done under this final stage are image denoising, where noise is minimized using sophisticated techniques, and further image enhancement. Fig. 1 in [11] illustrates the two steps of SR, namely registration and reconstruction. From the figure, sequence of images is captured in "A" and aligned in a common grid called sub-pixel grid in "B". The geometrical arrangement of pixels in a sub-pixel grid depends on the method used to capture the images. Finally, a sub-pixel grid is projected on a high resolution grid in "C". Following this simple and straightforward illustration, we can therefore divide SR algorithms into two major categories: registration and reconstruction algorithms. This paper examines the reconstruction algorithms. In order to complete the SR framework (see Fig. 1), and test the performance of our method, we use a registration algorithm by Vandewalle et al. [12] to estimate the roto-translation motions in a sub-pixel grid. Other registration algorithms, however, may be used to test the performance attributes of our method.
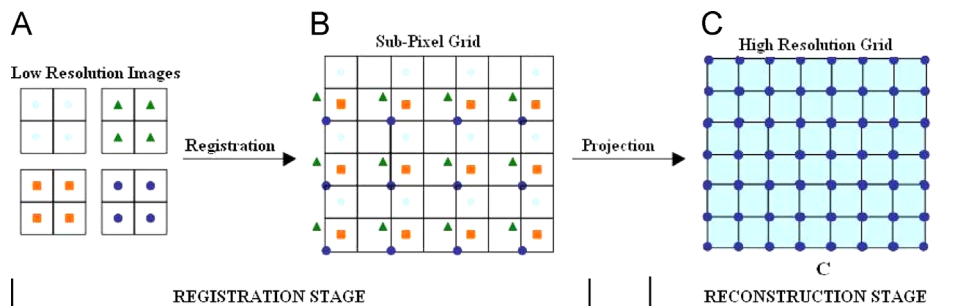
Fig. 1. Registration and reconstruction stages of SR.

One of the examples of the SR reconstruction method is called the RSR (robust super-resolution) method, which was originally realized by Zomet et al. [13]. This is an improved version of the Iterative Back Projection (IBP) method [14]. The major difference between the two methods relies on the computation of the optimal image gradient in the observation model. While the IBP computes the gradient by summation of the errors, the RSR uses the median of the errors. This makes the RSR more robust against the outliers in the LR images. The RSR method, just like the IBP method, is fast and can be easily understood, however, it does not efficiently solve the problem of loss of high-frequency spatial information caused by the imaging process operations. Furthermore, the method dramatically degrades its performance as reconstruction scaling factors get larger.

1.2. The SR observation model

The term observation model, in the context of an image reconstruction problem, can be defined as a framework which establishes the relationship between the desired HR image and the observed LR images [15]. This model shows all events a desired HR image undergoes from an instant it is acquired by an imaging device to the point it is observed as a LR image. The observation models can be broadly divided into two main parts, namely observation models for still images and for video sequence. In the discussion of this paper, we have employed the observation model for still images. However, it is straightforward to extend the idea to the video sequence model.

Fig. 2 illustrates a general structure of the SR observation model. In order to comprehensively understand this observation model, consider a desired HR image I of size $L_1 N_1 \times L_2 N_2$, where L_1 and L_2 are scaling factors and N_1 and N_2 are the pixel dimensions in the horizontal and vertical directions of the corresponding observed LR image. The image I is discrete and is obtained by sampling at Nyquist frequency (without aliasing) a continuous scene by sampler A. It then undergoes warping process in part B, which includes rotations and translations, to form a warped HR image I_k. The operation for warping an image I is performed by a warping matrix M_k. In part C, the image I_k is passed through a blurring function B_k. The blurring operator can be due to motion, sensor Point Spread Function (PSF) or optical characteristics. In part D, the resulting image from C is downsampled using a subsampling matrix D_k with factors L_1 and L_2. Finally, an additive noise N_k is added to an image in step E to form an observed image Z_k.
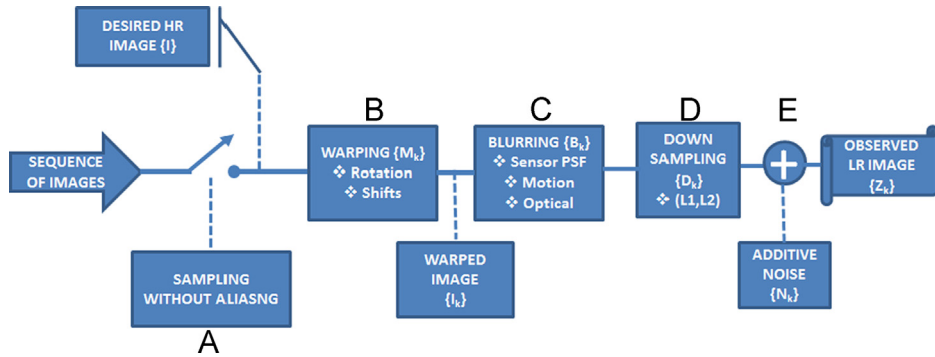
Fig. 2. The observation model for a SR reconstruction problem.

1.3. Background of SR methods

The RSR method presented in [13] was established using the concepts presented from [14,16,17]. It combines a robust median estimator in an iterative process to achieve a SR algorithm. Unlike other reconstruction methods, the RSR method applies a robust median-based estimator to disregard measurements which are not in agreement with the imaging model. With this technique, the RSR becomes more robust against motion errors, inaccurate blur models, moving objects and motion blur.

Consider a conceptual image formation model in [18] shown in Eq. (1), where $\overrightarrow{Z_k}$ is the kth input image reordered in a vector, D_k is the decimation matrix, B_k is the blurring matrix, M_k is the geometric warp matrix, $\overrightarrow{I}$ is the high resolution image reordered in a vector, and $\overrightarrow{N_k}$ is the normally distributed additive noise reordered in a vector:

$$\overrightarrow{Z_k} = D_k B_k M_k \overrightarrow{I} + \overrightarrow{N_k}. \tag{1}$$

The main objective is to minimize $\overrightarrow{N_k}$. Thus, the total error due to resampling of a high resolution image $\overrightarrow{I}$ is given by

$$L\left(\overrightarrow{I}\right) = \frac{1}{2} \sum_{k=1}^{n} \|\overrightarrow{Z_k} - D_k B_k M_k \overrightarrow{I}\|_2^2. \tag{2}$$

If we take the gradient of L with respect to $\overrightarrow{I}$, we get

$$\overrightarrow{P_k} = B_k^T M_k^T D_k^T (D_k B_k M_k \overrightarrow{I} - \overrightarrow{Z_k}),$$
$$\nabla L(\overrightarrow{I}) = \sum_{k=1}^{n} \overrightarrow{P_k}. \tag{3}$$

The optimum solution of Eq. (3) can be iteratively obtained using Eq. (4), where λ defines the step size in the direction of the gradient:

$$\overrightarrow{I}^{n+1} = \overrightarrow{I}^{n} + \lambda \nabla L(\overrightarrow{I}). \tag{4}$$

The IBP method uses (3) and (4) to approximate the high resolution image $\overrightarrow{I}$. In the case of the IBP method, estimation is done by iteratively resampling an assumed high resolution image in the lattice of the input images. Each time, the difference between the resampled image and the input image is calculated and projected back to the high resolution lattice. The RSR method undergoes very similar processes as the IBP method, only that it computes the error function differently. While the IBP method uses an error-summation estimator, the RSR method uses

error-median estimator. The robustness of the RSR method against the outliers of the input image sequence emanates from the way the error function is computed. In Eq. (5), the sum of the error function in Eq. (3) has been replaced by a scaled pixel-wise median to increase robustness:

$$\nabla L(\vec{I})(x, y) \approx n \times median\{\vec{P_k}(x, y)\}_k^n. \tag{5}$$

Our analysis on Eq. (5), using several experiments, indicates that the RSR method produces relatively nice results when a reconstruction factor of two is used. However, in typical real world applications, one would prefer to achieve higher resolutions from very low resolution images. In such a situation, higher reconstruction factors are required. The results from experiments further indicate that the RSR method does not perform well for this demand. The reason can be due to loss or degradation of high spectral components and amplification of errors and noise as the scaling factors get large. In [19], a method called *NCxx* that attempts to reconstruct HR images with significantly improved qualities at higher reconstruction factors was proposed. This method employs the strategies of Normalized Convolution (NC) [20], where estimation of a local function is achieved through a projection onto a subspace. Empirical results from *NCxx* show better results when compared to several classical methods, including the *PG* [11], *IBP* [14] and *POCS* [21]. The problems with this method, however, are larger computational times and lack of mechanisms to compensate for the lost details of an image as a result of low-pass filtering from the imaging model. In addition, the *NCxx* does not provide reliable solution for dealing with outliers and noisy data.

Recently, various regularization techniques have been proposed to solve a super-resolution problem. These methods incorporate some prior information into the existing SR models to address the challenge of ill-posedness encountered in several SR methods. In [22], for example, the authors propose a Total Variational (TV) prior (see [23,24]) based on Bayesian approach. The Bayesian TV SR method reconstructs a HR image while simultaneously performs noise removal and edge preservation. Similar approaches which also use Bayesian techniques were proposed in [25], where ℓ_1-norm was used as prior, and in [26], where ℓ_1-norm and SAR model combination is used. In spite of the advantages of simultaneously improving edges and removing noise during reconstruction process, SR regularized methods do not properly address the problem of aliasing effects and loss of high frequency components for hyper-resolved images. Motivated by these rather obvious challenges, we propose a method that can estimate missing structures of an image caused by degradation processes of an imaging model, and also regulates aliasing effects.

The proposed method improves the adaptive Perona–Malik (PM) regularization model [27], which is based on a traditional PM scheme [28], by incorporating a median filter for robust outlier detection. Moreover, our method provides an algorithm for estimating missing details and correcting aliasing effects. Several experiments performed demonstrates that the method produces stable and better results even at higher reconstruction factors.

The remainder of paper is sectionalized as follows. In Section 2, a proposed reconstruction method is provided. The experimental results are detailed in Section 3. The paper is concluded in Section 4 with recommendations and possible future research directions.

2. The proposed reconstruction method

2.1. High frequency components estimation and aliasing effects correction

Consider a band-limited signal, $I \in L^2(\mathbb{R})$, with some known knowledge about its bandwidth $[-\varpi \varpi]$. Then, by definition, the Fourier Transform (FT) of I, $I(\omega) = 0, \forall \omega \notin [-\varpi \varpi]$.

Consequently, $I(\omega)$ of I is finite and taken over a definition domain of I. In our situation, I is a 2D image and more specifically, consider I as an initial guess for an HR image in a simulated imaging process.

It is required to iteratively resample I and compare the resampled LR images to the observed LR images from the real imaging model, and then update I on the basis of the resulting effect of comparison. This process, however, has a disadvantage of causing degradation of the spatial characteristics and fine details of a final HR image. Because of this, category of SR methods which use this approach may not achieve better quality output images. The proposed method extends the applications of the methods proposed in [29,30] to solve the addressed challenges and limitations.

The engine of the algorithm can be explained as follows. An image signal is passed through a low-pass filter within the known bandwidth to assign values to its unknown pixels. Since the amplitudes of the known pixel values decrease as a result of low-pass filtering operation, a mechanism is developed to force these pixels to attain their original amplitudes. While in the frequency domain, the frequency components outside the passband are set to zero. As a result, a signal becomes no longer bandlimited. Furthermore, an automatic extrapolation of some of the high frequency components of an image is encountered. These steps are done iteratively until desired convergence is attained. Therefore, the proposed method can be summarized by Eq. (6), where β is constant, $\Gamma^{\eta}(\cdot)$ is the low-pass filtering operator of order η, $I(\varphi, \zeta)$ is the image (assumed to be continuous in this case), $\Xi(\cdot)$ is an operator that adjusts low-pass filtered amplitude values, and Υ is the simulated imaging process:

$$\psi(\varphi, \zeta) = \beta \left\{ \int_{\omega} \Xi \left(\Gamma^{\eta} \left(\int_{\Omega} I(\varphi, \zeta) e^{-j\omega\Omega} \, d\Omega \right) e^{j\omega\Omega} \right) d\omega \right\}_{\Upsilon}. \tag{6}$$

From Eq. (6), an image (updated HR image from a simulated imaging model) is initially passed through a low-pass filter and integrated over the image domain Ω. This is followed by forcing the pixel amplitudes to their original values and recovering a corresponding spatial domain image signal.

In order to transform Eq. (6) into a computer program to simulate and test the proposed algorithm, the following notations are used, and further Algorithm 1 is developed; $F(\cdot)$ is a Fourier Transform operator, $F^{-1}(\cdot)$ is a Inverse Fourier Transform operator, I_k is an updated estimate of a HR image, P_{ω} is a result of low pass filtering of an updated HR image in a frequency domain, P_{ω}^{Ψ} is P_{ω} with adjusted amplitude values, ω^* are frequency components outside an image defined bandwidth, and $\Xi(\cdot)$ is an operator that forces P_{ω} amplitude values to their original magnitudes.

Algorithm 1. The RS-HFCE engine.

Input: I_k
Output: I
  while $k \leq N$ **do**
    $I_k(\omega) = F(I_k)$
    $P_{\omega} = \Gamma^{\eta}(I_k(\omega^*))$
    $P_{\omega}^{\Psi} = \Xi(P_{\omega})$
    $I_k = F^{-1}(P_{\omega}^{\Psi})$
  end while
  return I

2.2. Regularization on RS-HFCE

Several drawbacks of non-regularized methods for solving a SR problem have already been discussed in Section 1. However, it is important to add that regularization approaches have been proposed from literatures, since they give promising solution to the challenges inherent in non-regularized methods. Of a large class of regularization methods available, PM [28] and TV [23,24] approaches have drawn more attention from various researchers. This is due to the capabilities these methods have in sharpening and enhancing crucial image features such as edges. Furthermore, the mathematical formulation of the TV and PM models can fairly be understood and analyzed. However, the TV regularization method suffers from false edge generation and staircase effects for images severely degraded by noise (see [31]) while PM regularization suffers from speckles in the final generated images. In [27], an adaptive approach is provided to automatically switch between the PM, linear isotropic diffusion [32], and Charbonnier [33] models, on the basis of the local image structures. Nevertheless, this method, despite its adaptive nature, still does not address and solve the problems attributed to either of the methods. The new method proposed in this paper introduces a regularizing median filter [34] into the model proposed in [27]. In comparison to other types of filters, such as the one recently discussed in [35], the median filter has been proved to have high performance against the outliers [36].

Now, we propose an evolution equation from which an optimal estimate of I can be determined. If we let $J_k(\cdot)$ be the transformation operator with entities B_k, M_k, D_k still as described in Section 1.3, an evolution equation which also takes into account the proposed algorithm in Section 2.1 can be realized in Eq. (7), where $\Gamma\{\cdot\}$ is the median operator, $\delta I = I - I_o$, functional R_m is defined in Eq. (8), $p(x)$ is an adaptive parameter with range of values determined by the local image features, and $\psi(\varphi, \zeta)$ is the high frequency component estimator shown in Eq. (6). The formulation of the RS-HFCE method in Eq. (7) is summarized in Fig. 3:

$$\frac{\partial I}{\partial t} = \sum_{k=1}^{n} \{(J_k^T(\vec{Z_k}) - J_k^T J_k(\vec{I}))\}_{\psi} + \gamma_1 n \Gamma \left\{ \nabla.R_m \left(\left[\frac{|\nabla I|}{K} \right]^{p(x)} \right) \right\} - \gamma_2 \delta I \qquad (7)$$

$$R_m(\cdot) = \frac{\nabla I}{1 + \left(\frac{|\nabla I|}{K} \right)^{p(x)}} \qquad (8)$$

The value of $p(x)$ is defined in a range $0 \leq p(x) \leq 2$ by the equation:

$$p(|\nabla G_\sigma * I|) = 2 - \frac{2}{1 + \kappa |\nabla G_\sigma * I|^2} [27] \qquad (9)$$

where G_σ is the Gaussian kernel.

It is easy to see that the regularization part of the formulation in Eq. (7) is either linear isotropic, similar to charbonnier, or PM, for values of $p(x)$ equal to 0, 1, and 2. This adaptive behavior, which is automatically controlled by Eq. (9), makes our method flexible, and thus providing an effective reconstruction while simultaneously preserving crucial image details, such as contours and edges.

2.3. Convergence criterion determination

Since the method is iterative, we must set a convergence condition to arrive at a solution. We realized from experiments that choice of a convergence condition also affects the results of
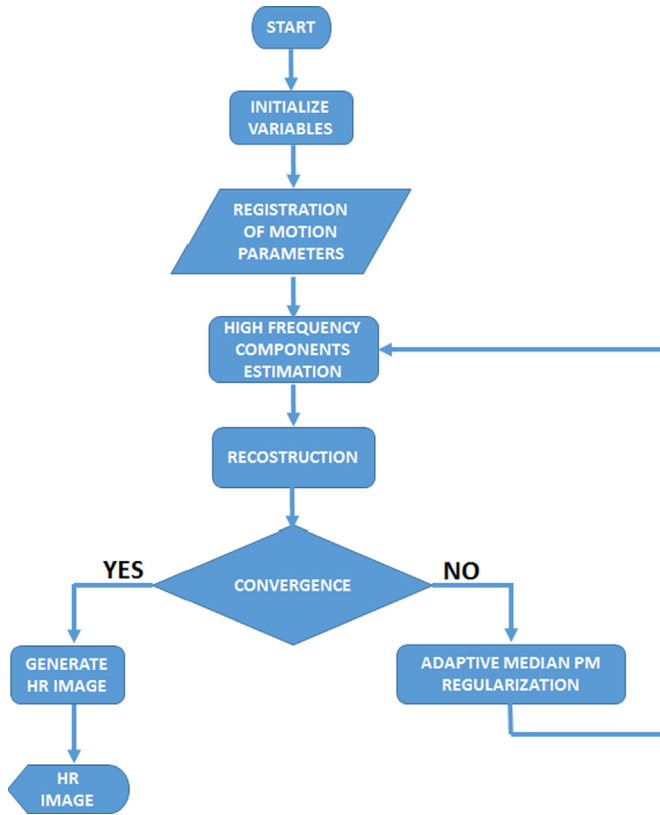
Fig. 3. Flow chart of the proposed algorithm.

the final solution. If not properly chosen, the whole iteration process of the algorithm may become unstable and in some cases one ends up with far too many iterations, unnecessarily. In our method, we use a Mean Structural SIMilarity (MSSIM) [37] aspect, unlike the norm-2 criterion used by other reconstruction methods, as a convergence condition for two main reasons. One, it integrates parameters which simulate the Human Vision System (HVS) and two, it proved to converge to a final solution faster compared to the norm-2 convergence criterion. The norm-2 convergence criterion did not provide reliable and stable results in particular cases, especially when large reconstruction scaling factors were used.

Let $MSSIM(I^n, I^{n-1})$ be the Mean Structural Similarity measure between two images, I^n and I^{n-1}, then the convergence condition can be defined by Eq. (10), where ε is an convergence error limit and $dist(\cdot)$ is a positive distance operator:

$$dist(1 - MSSIM(I^n, I^{n-1})) < \varepsilon. \tag{10}$$

The *MSSIM* is defined by Eq. (11), where μ_{i^n} and $\mu_{i^{n-1}}$ are the averages, and $\sigma^2_{i^n}$ and $\sigma^2_{i^{n-1}}$ are the variances, and $\sigma_{i^n i^{n-1}}$ is the covariance, of I^n and I^{n-1}, respectively. The constants, C_1 and C_2, are used to stabilize the division with weak denominator

$$MSSIM\left(I^n, I^{n-1}\right) = \frac{(2\mu_{i^n}\mu_{i^{n-1}} + C_1)(2\sigma_{i^n i^{n-1}} + C_2)}{(\mu^2_{i^n} + \mu^2_{i^{n-1}} + C_1)(\sigma^2_{i^n} + \sigma^2_{i^{n-1}} + C_2)}. \tag{11}$$

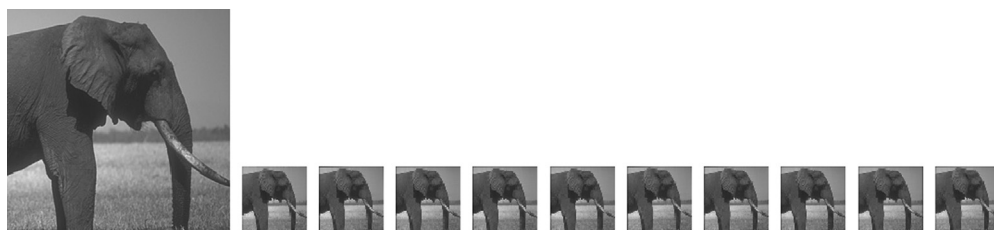Fig. 4. Decomposition of a HR image of a Pot into sequence of LR images.

Fig. 5. Decomposition of a HR image of an Elephant into sequence of LR images.

The boundaries of an *MSSIM* measure are between zero and one inclusive. The maximum value is one when the images under comparison are exactly equal (100% match) and, when the match is 0%, the *MSSIM* index value is zero.

3. Experiment results[1]

In this section, we present summary of the experimental results along with the comparison made between our method and the state of the art methods L1-SAR [26], TV-SR [22], and L1-Norm [25]. Quantitative comparison results using the Peak Signal to Noise Ratio (PSNR) and Mean Structural SIMilarity (MSSIM) are also given. In addition, convergence speed of each of the methods is determined using the overall CPU computational time and the total number of iteration an algorithm takes to attain an optimal solution. Using this measuring criteria, we intuitively determine whether a given method converges or diverges from an actual solution. The machine we used in all experiments was Intel(R) Core(TM)2 Duo CPU T5870 @2.00 GHz running on 64-bit Windows 7 Professional, and installed RAM of 2 GB. The software used to generate results of the methods L1-SAR, TV-SR and L1-Norm was taken from [38]. Notice that, in this software, the deconvolution type chosen was Gaussian of variance 1.00 and kernel size of 3, and the MODE/RESET type selected was *Real*.

In the first experiment, ten sequences of LR images of Pots, each 60×60 pixel dimension and simulated rotations and translations, were generated from a corresponding real HR image of a Pot of dimension 240×240 (see Fig. 4). The methods L1-SAR, TV-Prior, L1-Norm and RS-HFCE, one after another, were applied to reconstruct a HR image for scaling factors of two and four. The second experiment involved similar procedures, but using an Elephant image (see Fig. 5). The super-resolution results for the two sets of experiments are illustrated in Tables 1 and 2.

---

[1]Images taken from Berkeley benchmark: http://www.eecs.berkeley.edu/Research/Projects/CS/vision/grouping/segbench/

Table 1
SR results for different methods (factor=two). Images scaled to page.
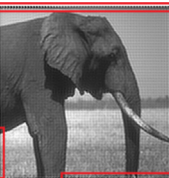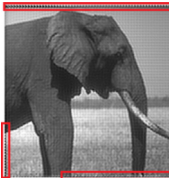
Original image	Method			
	L1-Norm	TV-Prior	L1-SAR	RS-HFCE

Table 2
SR results for different methods (factor=four). Images scaled to page.

Original image	Method			
	L1-Norm	TV-Prior	L1-SAR	RS-HFCE

From the tables, red-colored markings were added in portions of the images which indicated some obvious visible artifacts. We can see that the visual results from figures show that the proposed method outperforms other methods. The images generated by the new method are smooth and more natural.

In order to quantify the performance of our method, the PSNR and MSSIM for each of the methods were computed as illustrated in Tables 3 and 4, respectively, under different conditions of the experiments. We can see from the table of results that the RS-HFCE provides higher PSNR and MSSIM values in comparison to the L1-SAR, TV-Prior and L1-Norm methods. It should be noted that higher PSNR signals higher signal content in the super-resolved image, and

Table 3
PSNR comparison results table.

Image	Factor	PSNR			
		L1-SAR	TV-Prior	L1-Norm	RS-HFCE
Pot	2	14.2148	13.2317	13.6033	27.8150
	4	14.6794	14.4691	14.4859	28.1117
Elephant	2	19.3595	18.1116	17.7153	25.0805
	4	20.9133	20.2947	20.3466	26.0934
Mean		17.2918	16.5268	16.5378	26.7752
Standard deviation		3.3508	3.2558	3.0938	1.4381

Table 4
MSSIM comparison results table.

Image	Factor	MSSIM			
		L1-SAR	TV-Prior	L1-Norm	RS-HFCE
Pot	2	0.6536	0.3583	0.4863	0.8370
	4	0.6762	0.5848	0.5769	0.8138
Elephant	2	0.7503	0.6174	0.5732	0.8168
	4	0.7119	0.6172	0.6190	0.7235
Mean		0.6980	0.5444	0.5638	0.7978
Standard deviation		0.0423	0.1250	0.0557	0.0506

higher MSSIM index means that the final output image is close to the original image in terms of the visual perception of the human vision system.

We also performed the computational complexity analysis of the proposed method and compared it with other methods. Two main aspects were used in this case, namely the CPU running time and the effective number of iteration for a given algorithm to complete execution and generate the final result. As it can be observed in the analysis (Table 5), the RS-HFCE method takes shorter time and uses relatively lower number of iterations to complete execution. In addition to this analysis, we observed the stability and convergence issues of the intermediate results of the methods during the iteration processes. This was, however, judged subjectively as high, low, or lowest, depending on the behavior of the experiments in the generation of the intermediate results. We realized that the intermediate images produced by the proposed method were stable in all conditions of the experiment. This means that, starting from the minimum iteration number, the generated images were linearly improving. On the other hand, the relationship of the scale space images of other methods was observed to be inconsistent and nonlinear. For instance, in some situations an image I^n was visually poor than an image I^{n-1}. The stability subjective analysis for various methods is also shown in Table 5.

Lastly, we performed experiments to reconstruct a HR image from a set of ten colored LR images of Pots (see Fig. 6) for reconstruction factors of six, eight, nine and ten. The methods L1-SAR,

Table 5
Computational complexity and stability analysis table.

Image	Factor	Attribute	Method			
			L1-SAR	TV-Prior	L1-Norm	RS-HFCE
Pot	2	No. iteration	26	>82	82	5
		CPU time (s)	573.3679	1848.9651	1604.6802	7.4305
		Stability	High	Lowest	Lowest	High
	4	No. iteration	51	58	64	5
		CPU time (s)	2199.5002	2752.6595	2935.7636	28.2871
		Stability	Medium	Low	Low	High
Elephant	2	No. iteration	24	35	52	5
		CPU time (s)	445.0268	719.5215	951.6411	4.0203
		Stability	High	Medium	Medium	High
	4	No. iteration	47	70	73	5
		CPU time (s)	3713.5331	3290.7645	2945.4689	10.1120
		Stability	High	Medium	Medium	High

Fig. 6. Sequence of ten colored LR images of POTS, each 60×60, with simulated roto-translation parameters. (For interpretation of the references to color in this figure caption, the reader is referred to the web version of this paper.)

Fig. 7. Reconstruction using RS-HFCE method for factors (a) six, (b) eight, (c) nine, and (d) ten. Images are $\times 0.15$ scaled to page.

TV-Prior and L1-Norm did not work for this condition. The RS-HFCE method, on the other hand, showed better results for these higher reconstruction factors. From Fig. 7, one can see that the output HR images generated using the RS-HFCE maintain their local structures and visual artifacts are considerably low. The quantitative results from Table 6 demonstrate capabilities of the proposed method under these conditions.

Table 6
Results table of RS-HFCE using factors six, eight, nine and ten.

Image	Factor	No. iteration	CPU time (s)	PSNR	MSSIM
POT	6	5	23.6104	25.4608	0.6178
	8	6	54.0892	25.0874	0.5997
	9	6	65.1582	24.9704	0.6058
	10	7	103.2732	24.8907	0.5994
Mean			61.5328	25.1023	0.6057
Standard deviation			32.9086	0.2523	0.0086

4. Conclusion

A more efficient and robust reconstruction technique for recovering fine details of a final HR image has been proposed in this paper. The method takes advantage of the definition of low-pass filtering in a high-resolution lattice to interpolate the unknown pixel values in the lattice, thus correcting the aliasing for the low frequency components. In order to approximate the values of the high frequency components in the grid, a low-pass filtering process was done along with forcing the amplitude values of the known pixel components. In addition, the proposed method incorporates an improved adaptive Perona–Malik regularization model into the SR degradation model to sharpen and enhance edges of the output images. Several experiments performed, some of which are presented in this paper, provide a proof, both from the visual appeal and objective metrics perspectives, that our method outperforms most of the classical SR reconstruction methods.

A few research opportunities are available as noted from this research work. Firstly, due to convergence criterion used, it might be interesting to explore the performance of the proposed method when implemented in real hardware platforms. The MSSIM convergence criterion provides quick, stable and reliable convergence as practically observed from various types of experiments. Secondly, we can extend the method to video applications. This will involve generation of High Definition (HD) video from low resolution video. The proposed method has proven higher orders of reconstruction at minimum degradation levels, which provides a hope to reconstruct beyond high definition movies from noisy and low-resolution video frames. Lastly, output images observed using the proposed method contain some blur information and the contrast is relatively low. We can improve the current results if a proper deblurring model is incorporated into our method.

References

[1] S. Park, M. Park, M. Kang, Super-resolution image reconstruction: a technical overview, IEEE Signal Processing Magazine 20 (2003) 21–36.

[2] S. Salehi, H. Mahdavi-Nasab, New image interpolation algorithms based on dual-tree complex wavelet transform and multilayer feedforward neural networks, International Journal of Innovative Computing, Information and Control 8 (2012) 6885–6902.

[3] W.-C. Siu, K.-W. Hung, Review of image interpolation and super-resolution, in: Signal & Information Processing Association Annual Summit and Conference (APSIPA ASC), 2012 Asia-Pacific, IEEE, pp. 1–10.

[4] D. Kanellopoulos, P. Lalos, G. Tombras, Implementing a zoomable web browser with annotation features for managing libraries of high quality images, International Journal of Innovative Computing, Information and Control 8 (10(B)) (2012) 7225–7235.

[5] S. Yin, X. Yang, H.R. Karimi, Data-driven adaptive observer for fault diagnosis, Mathematical Problems in Engineering 2012 (2012).

[6] S. Ding, S. Yin, K. Peng, H. Hao, B. Shen, A novel scheme for key performance indicator prediction and diagnosis with application to an industrial hot strip mill, Paper no. TII-12-0329, IEEE, 2009.

[7] S. Yin, S.X. Ding, A.H. Abandan Sari, H. Hao, Data-driven monitoring for stochastic systems and its application on batch process, International Journal of Systems Science 44 (2013) 1366–1376.

[8] S. Yin, S.X. Ding, A. Haghani, H. Hao, P. Zhang, A comparison study of basic data-driven fault diagnosis and process monitoring methods on the benchmark tennessee eastman process, Journal of Process Control 22 (9) (2012) 1567–1581, http://dx.doi.org/10.1016/j.jprocont.2012.06.009.

[9] D. Glasner, S. Bagon, M. Irani, Super-resolution from a single image, in: 2009 IEEE 12th International Conference on Computer Vision, IEEE, pp. 349–356.

[10] B. Zitova, J. Flusser, Image registration methods: a survey, Image and Vision Computing 21 (2003) 977–1000.

[11] D. Jain, Superresolution using Papoulis-Gerchberg algorithm, EE392J Digital Video Processing. Stanford University, Stanford, CA, 2005.

[12] P. Vandewalle, L. Sbaiz, J. Vandewalle, M. Vetterli, Super-resolution from unregistered and totally aliased signals using subspace methods, IEEE Transactions on Signal Processing 55 (2007) 3687–3703.

[13] A. Zomet, A. Rav-Acha, S. Peleg, Robust super-resolution, in: Proceedings of the 2001 IEEE Computer Society Conference on Computer Vision and Pattern Recognition, 2001 (CVPR 2001), vol. 1, IEEE, pp. 1–645.

[14] M. Irani, S. Peleg, Improving resolution by image registration, CVGIP: Graphical Models and Image Processing 53 (1991) 231–239.

[15] S. Qureshi, X. Li, T. Ahmad, Investigating image super resolution techniques: What to choose?, in: 2012 14th International Conference on Advanced Communication Technology (ICACT), IEEE, pp. 642–647.

[16] M. Irani, S. Peleg, Super resolution from image sequences, in: Proceedings of 10th International Conference on Pattern Recognition, 1990, vol. 2, IEEE, pp. 115–120.

[17] D. Keren, S. Peleg, R. Brada, Image sequence enhancement using sub-pixel displacements, in: Proceedings of IEEE Computer Society Conference on Computer Vision and Pattern Recognition (CVPR'88), 1988, pp. 742–746.

[18] M. Elad, A. Feuer, Restoration of a single superresolution image from several blurred, noisy, and undersampled measured images, IEEE Transactions on Image Processing 6 (1997) 1646–1658.

[19] Q. Pham Tuan, J. van Vliet Lucas, Robust fusion of irregularly sampled data using adaptive normalized convolution, EURASIP Journal on Applied Signal Processing (2006), http://dx.doi.org/10.1155/ASP/2006/83268, in press.

[20] H. Knutsson, C.-F. Westin, Normalized and differential convolution, in: Proceedings of IEEE Computer Society Conference on Computer Vision and Pattern Recognition, 1993 (CVPR'93), 1993, IEEE, pp. 515–523.

[21] H. Stark, P. Oskoui, High-resolution image recovery from image-plane arrays, using convex projections, Journal of the Optical Society of America A 6 (1989) 1715–1726.

[22] S. Babacan, R. Molina, A.K. Katsaggelos, Variational bayesian super resolution, IEEE Transactions on Image Processing 20 (2011) 984–999.

[23] P. Getreuer, Rudin-osher-fatemi total variation denoising using split bregman, Image Processing On Line (2012).

[24] L.I. Rudin, S. Osher, E. Fatemi, Nonlinear total variation based noise removal algorithms, Physica D: Nonlinear Phenomena 60 (1992) 259–268.

[25] S. Villena, M. Vega, R. Molina, A. K. Katsaggelos, Bayesian super-resolution image reconstruction using an l1 prior, in: Proceedings of 6th International Symposium on Image and Signal Processing and Analysis, 2009 (ISPA 2009), IEEE, pp. 152–157.

[26] S. Villena, M. Vega, S. Babacan, R. Molina, A. Katsaggelos, Bayesian combination of sparse and non sparse priors in image super resolution, Digital Signal Processing (2012), http://dx.doi.org/10.1016/j.dsp.2012.10.002, in press.

[27] Z. Guo, J. Sun, D. Zhang, B. Wu, Adaptive Perona–Malik model based on the variable exponent for image denoising, IEEE Transactions on Image Processing 21 (2012) 958–967.

[28] P. Perona, J. Malik, Scale-space and edge detection using anisotropic diffusion, IEEE Transactions on Pattern Analysis and Machine Intelligence 12 (1990) 629–639.

[29] A. Papoulis, A new algorithm in spectral analysis and band-limited extrapolation, IEEE Transactions on Circuits and Systems 22 (1975) 735–742.

[30] R. Gerchberg, Super-resolution through error energy reduction, Journal of Modern Optics 21 (1974) 709–720.

[31] S. Oh, H. Woo, S. Yun, M. Kang, Non-convex hybrid total variation for image denoising, Journal of Visual Communication and Image Representation 24 (2013) 332–344.

[32] J. Weickert, A review of nonlinear diffusion filtering, in: Scale-space Theory in Computer Vision, Springer, 1997, pp. 1–28.

[33] P. Charbonnier, L. Blanc-Feraud, G. Aubert, M. Barlaud, Two deterministic half-quadratic regularization algorithms for computed imaging, in: Proceedings of IEEE International Conference on Image Processing, 1994 (ICIP-94), vol. 2, IEEE, pp. 168–172.

[34] M.J. Mane, M. Chavan, Design and implementation of median filter for image denoising, International Journal of Electrical and Electronic Engineering and Telecommunications 2 (2) (2013).

[35] A. Chaudhry, J.Y. Kim, T.A. Tuan, Improved adaptive fuzzy punctual kriging filter for image restoration, International Journal of Innovative Computing, Information and Control 9 (2) (2013) 583–598.

[36] S.-J. Horng, L.-Y. Hsu, T. Li, S. Qiao, X. Gong, H.-H. Chou, M. K. Khan, Using sorted switching median filter to remove high-density impulse noises, Journal of Visual Communication and Image Representation, 2013, http://dx.doi.org/10.1016/j.jvcir.2013.06.012, in press.

[37] Z. Wang, A. Bovik, H. Sheikh, E. Simoncelli, Image quality assessment: from error visibility to structural similarity, IEEE Transactions on Image Processing 13 (2004) 600–612.

[38] Super-resolution software, ⟨http://decsai.ugr.es/pi/superresolution/software.html⟩, 2012 (accessed 29.02.2013).